Supplementary Information

Multicationic $Sr_4Mn_3O_{10}$ mesostructures: molten salt synthesis, analytical electron microscopy study and reactivity

Irma N. González-Jiménez,[a] Almudena Torres-Pardo,[a,b] Simon Rano,[c] Christel Laberty-Robert,[c] Juan Carlos Hernández-Garrido,[d,e] Miguel López-Haro,[d,e] José J. Calvino,[d,e] Áurea Varela,[a] Clément Sanchez,[c] Marina Parras,[a,*] José M. González-Calbet,[a,f] David Portehault[c,*]

[a.] *Departamento de Química Inorgánica, Facultad de CC. Químicas, Universidad Complutense de Madrid, 28040 Madrid, Spain,E-mail: mparras@quim.ucm.es*
[b.] *CEI Campus Moncloa, UCM-UPM, Madrid, Spain.*
[c.] *Sorbonne Université, CNRS, Collège de France, Laboratoire Chimie de la Matière Condensée de Paris, LCMCP, 4 Place Jussieu, F-75005 Paris, France. E-mail: david.portehault@sorbonne-universite.fr*
[d.] *Departamento de Ciencia de los Materiales e Ingeniería Metalúrgica y Química Inorgánica, Facultad de Ciencias, Universidad de Cádiz, Campus Río San Pedro S/N, Puerto Real 11510 (Cádiz), Spain.*
[e.] *Instituto Universitario de Investigación de Microscopía Electrónica y Materiales (IMEYMAT). Facultad de Ciencias. Universidad de Cádiz. Campus Río San pedro S/N, Puerto Real 11510 (Cádiz), Spain.*
[f.] *Centro Nacional de Microscopía Electrónica, Universidad Complutense, 28040 Madrid, Spain*.

MOVIE S1. STEM-HAADF tomography of platelet, showing the crystalline component (blue) and the amorphous one (gold).

MOVIE S2. STEM-HAADF tomography of platelet, showing separately the crystalline component (blue) and the amorphous one (gold).

MATERIALS AND METHODS

Materials. $Sr(OH)_2 \cdot 8H_2O$, $KMnO_4$ and HNO_3 were purchased from Sigma-Aldrich. All chemicals were used as received. Water was purified through a Milli-Q Millipore system.

Synthesis. $Sr(OH)_2 \cdot 8H_2O$ and $KMnO_4$ (99+ %) were mixed in a molar ratio 65:1 (0.19 mmol of $KMnO_4$) and ground finely with a Retsch MM400 ball mill (airtight vials of 50 mL, one ball of 62.3 g and a diameter of 23 mm) for 2 min at 60 Hz. The resulting powder was transferred in a glassy carbon crucible, dehydrated in a vacuum oven at 40 ºC overnight and then heated at 600 ºC under Ar flow and Schlenk line conditions. Water evolved at *ca.* 300 °C. After being cooled down to room temperature, the obtained powders were dissolved in argon-saturated water to which HNO_3 (69%) was added dropwise until pH~5 was reached. The final powder was recovered after centrifugation, washed with Ar-saturated water 4 times and dried at 40 ºC in a vacuum oven. The final yield is *ca.* 80 %.

Scanning electron microscopy (SEM). SEM micrographs were acquired in a JEOL JSM 6335-FEG scanning microscope operating at an acceleration voltage of 5 kV.

Selected Area Electron Diffraction (SAED) and High Resolution Transmission Electron Microscopy (HRTEM) were performed on a JEOL 300FEG electron microscope. Chemical composition of the mesocrystals was determined by energy-dispersive **X-ray spectroscopy (EDS)** in both JEOL JSM6335-FEG and JEOL 300FEG electron microscopes. Mn-Kα_1 and Sr-K α_1 spectral lines were used for determination of Sr:Mn molar ratio over 30 particles. Standard deviations for the Sr:Mn ratios indicated in Figure 1J are 1.4 in areas 1 and 2; 3.9 in area 3. Atomic resolution images were acquired on a JEOL JEMARM200cF electron microscope (Cold Emission Gun) with a spherical aberration corrector in the probe (current emission density ~$1.4 \cdot 10^{-9}$ Å and probe size ~0.08 nm), coupled with a GIF-QuantumER spectrometer. We operated at 200 kV for pure $Sr_4Mn_3O_{10}$ samples and at 80 kV for those samples before washing. Solid semi-angles between 68–280 mrad were used for acquisition of HAADF images (38 s per frame). Atomically-resolved **Electron Energy Loss Spectroscopy (EELS)** maps were acquired with a spatial resolution ~0.1 nm, over a total acquisition time ~2 min (current emission density of ~1.2×10^8 A and a probe size of ~0.12 nm). Principal component analysis (PCA) with 8 components was performed on EELS data set to de-noise the spectra by using the Hyperspy data analysis toolbox. The Mn oxidation state was analyzed from the Energy-Loss Near-Edge fine Structure (ELNES) of Mn-$L_{2,3}$ signals. High energy resolution punctual EELS spectra were acquired over ~0.5 nm area with energy dispersion of 0.1 eV and 2 mm spectrometer aperture. The total acquisition time was optimized to 10 s in order to prevent beam-damage of the sample. Dual-EELS function of the GIF-QuantumERTM spectrometer, allowing the simultaneous acquisition of two different energy ranges, was used to record simultaneously the zero-Loss peak (10^{-4} s exposition time, 10 frames) and the Mn-$L_{2,3}$ core-region (1 s exposition time, 10 frames) in order to minimize the uncertainty on the energy shift of the Mn-$L_{2,3}$ edges. With the aim of analyzing the EELS experimental data obtained from the $Sr_4Mn_3O_{10}$ sample, EELS spectra were recorded from three valence standard samples: $Ca_2Mn_3O_8$ (Mn IV), $LaMnO_3$ (Mn III) and $Ca_2Mn_3O_5$ (Mn II).

Electron tomography experiments based on high-angle annular dark-field (HAADF) imaging in the scanning transmission electron microscopy (STEM) mode were performed on a JEOL 2010F electron microscope tilting the sample ±76° about a single axis using a Fischione 2030 ultra-narrow gap tomography holder. Tomography experiments based on high-angle annular dark-field (HAADF) imaging in the scanning transmission electron microscopy (STEM) mode were performed on a JEOL 2010F electron microscope operating at 200kV .The sample was tilted ±76° about a single axis using a Fischione 2030 ultranarrow gap tomography holder. Tilt series were aligned using Inspect3D software and reconstructed by Compressed Sensing technique. In particular, Total Variation Minimization (TVM) was carried out using the TVAL3 solver (C. Li,

Rice University, 2010) with projections and back-projections operators from the ASTRA Toolbox (W. van Aarle, W. J. Palenstijn, J. De Beenhouwer, T. Altantzis, S. Bals, K. J. Batenburg, and J. Sijbers, *Ultramicroscopy*, 2015, **157**, 35–47.), using GPU implementation for gain in rapidity. The reconstructed volume was thereafter segmented automatically using Multi-Otsu threshold implemented in Matlab and Amira software was used to visualize the 3D volume.

X-ray diffraction (XRD). XRD patterns were obtained by using a Panalytical X'Pert Pro Alpha1 instrument, equipped with a primary fast X'Celerator detector operating at 45 kV and 40 mA, and fitted with a primary curved Ge 111 monochromator in order to get the Cu $K_{\alpha 1}$ radiation (λ = 1.5406 Å). Data were collected at 2θ between 5º and 70º, with a step size of 0.04º and a collection time of 1 sec/step at room temperature.

Electrochemical characterization. The rotating disk electrode (RDE) was prepared by coating a glassy carbon (GC) disk electrode (0.07 cm², Radiometer Analytical) previously polished with diamond paste (1 µm, BAS inc.) followed by alumina paste (0.05 µm, BAS inc.) to reach mirror grade. A conductive ink containing the catalyst was then coated over the substrate:

Ink preparation. This ink was prepared from three components: the catalyst powder, Acetylene Black (AB, Alfa Aesar) (99.9+ %, 75 $m^2 \cdot g^{-1}$) and Nafion-117 solution (5% in aliphatic alcohol, Sigma-Aldrich). The Nafion-117 solution was previously ion-exchanged with Na^+ by slowly adding 1 mL of NaOH 0.1 M solution to 2 mL of Nafion alcoholic solution under stirring, followed by stirring during 5 minutes. The acetylene black powder was hydrophilized by dispersing 500 mg of AB in 50 mL of HNO_3 20 % at 80 °C overnight under stirring, followed by centrifugation and washing with water and vacuum drying. The ink was prepared by dispersing 10 mg of catalyst powder in 10 mL of ethanol (99%), along with 10 mg of treated AB. The mixture was sonicated in a water bath for 2 hours. Then, the dispersion was cooled to room temperature and dispersed with a sonic horn for 5 minutes. 347 µL of ion-exchanged Nafion solution was then added immediately. The ink was sonicated for 5 minutes and remained stable and aggregate free for at least 1 week.

Electrode preparation. After few minutes of horn sonicating in cool conditions, 1 µL of the ink was deposited on the GC substrate. The film was dried in a closed beaker for 20 min. Then, the electrode was transferred in an oven where it was dried for 1 hour at 60 °C. The prepared electrode consisted in a black film coated on the GC RDE with an oxide content of 15 $\mu g \cdot cm^{-2}_{disk}$.

Electrochemical characterization. The freshly prepared electrode was characterized with a three-electrode setup, with the RDE as the working electrode, a Pt wire as counter electrode and a Ag/AgCl electrode as reference. The setup was connected to a Solartron Analytical device potentiostat. Prior to electrochemical experiments, the working electrode was hydrated with the 0.1 M KOH electrolyte over 20 min. All cyclic voltammetry experiments were performed in either O_2 or N_2 (Air Liquid) saturated electrolyte at a scan rate of 10 $mV \cdot s^{-1}$. Capacity-corrected currents were obtained by averaging the potential over each reduction-oxidation cycle. To normalize the current versus the oxide surface, the specific surface area was evaluated at 6 $m^2 \cdot g^{-1}$ for $Sr_4Mn_3O_{10}$ according to geometrical calculations. Each experiment was repeated at least 3 times.

MUSIC^2 model. The charge of the different facets was evaluated by adapting the MUSIC^2 model (T. Hiemstra, W. Riemsdijk, G. H. Bolt, Multisite Proton Adsorption Modeling at the Solid/Solution Interface of (hydr)oxides: a new approach. I. Model Description and Evaluation of Intrinsic Reaction Constants. *J. Colloid Interf. Sci.* **133**, 91 (1989); T. Hiemstra, P. Venema, W. Riemsdijk, Intrinsic Proton Affinity of Reactive Surface Groups of Metal (Hydr)oxides: the Bond Valence Principle. *J. Colloid Interf. Sci.* **184**, 680–692 (1996)). The model considers effective valences *s* (L. Pauling, The Principles determining the Structure of Complex Ionic Crystals. *J. Am. Chem. Soc.* **51**, 1010 (1929)) of metal-oxygen bonds s_{Me} from Brown's and Altermatt's approach (I. D. Brown, I. D. Altermatt, Bond-Valence Parameters obtained from a Systematic Analysis of the Inorganic Crystal Structure Database. *Acta Cryst.* **B41**, 244 (1985)):

$$s = \exp[(r_0\text{-r})/B]$$

where r is the bond length, r_0 and B are empirical parameters (I. D. Brown, I. D. Altermatt, Bond-Valence Parameters obtained from a Systematic Analysis of the Inorganic Crystal Structure Database. *Acta Cryst.* **B41**, 244 (1985)):

$r_0(Mn^{4+}\text{-O}) = 1.753$ Å; $r_0(Sr^{2+}\text{-O}) = 2.118$ Å; $B(Mn^{4+}\text{-O}) = 0.370$; $B(Sr^{2+}\text{-O}) = 0.370$.

In bulk crystals, the electroneutrality principle implies that the sum of effective bond valences for a given atom and its valence (oxidation state) V is equal to 0. However, surface atoms experience frustrated coordination, so that the residual charge q on the surface group is equal to the sum of its effective bond valences (s) and its oxidation state:

$$q = V + \sum s$$

For hydroxo and oxo groups, the following equations apply:

$$q_{OH} = -1 + \sum s_{Me}$$

$$q_O = -2 + \sum s_{Me}$$

Where s_{Me} is the effective bond valence of each metal-oxygen bond. The model can also take into account charge transfer due to hydrogen bonds and yields similar expressions in our case (I. D. Brown, Geometry of O-H...O Hydrogen bonds. *Acta Cryst.* **A32**, 786 (1976)).

The MUSIC[2] model (T. Hiemstra, W. Riemsdijk, G. H. Bolt, Multisite Proton Adsorption Modeling at the Solid/Solution Interface of (hydr)oxides: a new approach. I. Model Description and Evaluation of Intrinsic Reaction Constants. *J. Colloid Interf. Sci.* **133**, 91 (1989); T. Hiemstra, P. Venema, W. Riemsdijk, Intrinsic Proton Affinity of Reactive Surface Groups of Metal (Hydr)oxides: the Bond Valence Principle. *J. Colloid Interf. Sci.* **184**, 680–692 (1996)) uses the residual charge q to evaluate the acidity constant of each aquo, hydroxo and oxo surface groups. In our case, the following equations apply:

$$pK_A^{HO/O} = -19.8\ (q_O)$$

$$pK_A^{H2O/OH} = -19.8\ (q_{OH})$$

By using this acidity constant, the surface density of each oxo and hydroxo group can be evaluated as a function of pH. By combining these speciation curves with the corresponding residual charges q, a theoretical evolution of the surface charge as a function of the pH can be retrieved. In highly basic media, aquo groups are unlikely to exist, so that we focused only on hydroxo, oxo groups and the first acidity constant $pK_A^{HO/O}$. Importantly, the model does not take into account electrostatic repulsions between neighbouring charged surface groups. Accordingly, experimental surface charge densities are lower than those retrieved from the model. Therefore, calculated values of charge densities should not be used for quantitative purpose but only for comparison between the different facets.

Although the model was originally developed to account for oxide surfaces in contact with water, it may still be applied in molten hydroxide, bearing in mind that the actual "pH" value should be adjusted to yield the highest amount of μ_1 (oxygen bonded to one metal cation), and μ_2 (oxygen bridging 2 metal cations) hydroxo groups bonded to surface Sr^{2+} ions. On the contrary, μ_4 hydroxo groups are unlikely because electron density on oxygen ions is strongly dragged by neighbouring metal cations. These considerations lead to focus studies on the highlighted "pH" area in **Figure S10**, between "pH" 20 and 30.

FIGURES

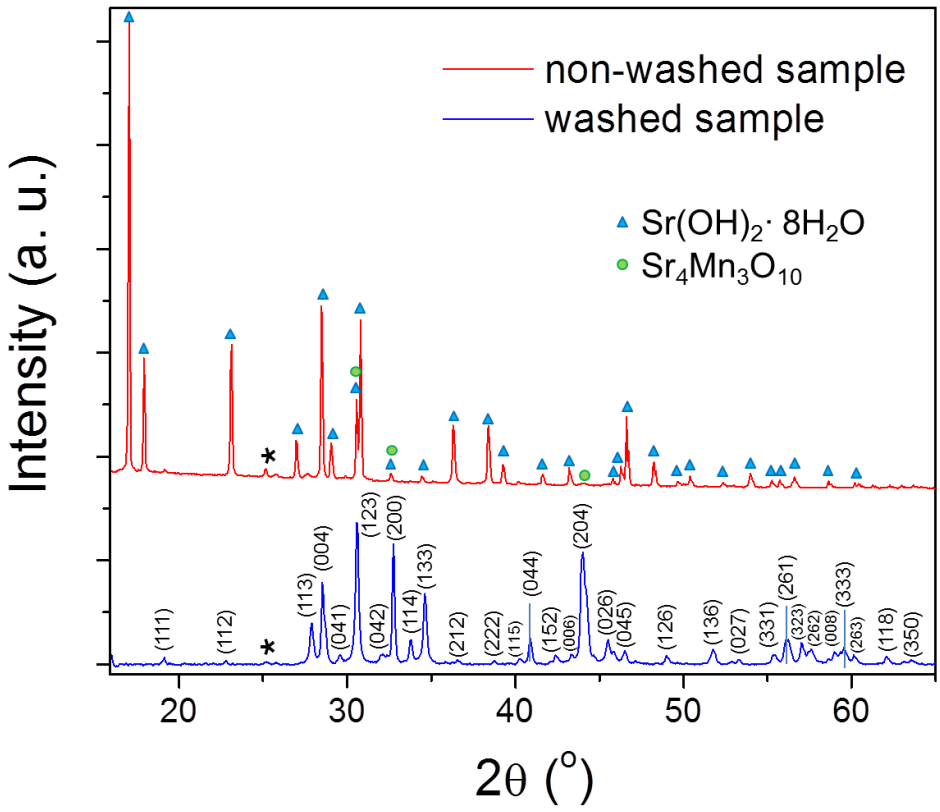

Figure S1. XRD patterns of the crude reaction medium at room temperature and exposed to air (red) and a sample washed with HNO_3 (blue). $Sr_4Mn_3O_{10}$ is always obtained after washing, as seen in (blue pattern) where all the maxima can be assigned to an orthorhombic cell of the *Cmca* space group. Experimental cell parameters $a = 0.547$ nm, $b = 1.238$ nm, $c = 1.251$ nm are in good agreement with the reference ones $a = 0.544$ nm, $b = 1.243$ nm, $c = 1.250$ nm (J. Fábry et al., Preparation and the crystal structure of a new manganate, $Sr_4Mn_3O_{10}$. *J. Solid State Chem.* **73**, 520–523, 1988 and N. Floros, M. Hervieu, G. van Tendeloo, C. Michel, A. Maignan, and B. Raveau, The layered manganate $Sr_{4-x}Ba_xMn_3O_{10}$: synthesis, structural and magnetic properties. *Solid State Sci.*, 1998, **2**, 1–9). Prior to washing (red pattern), it is possible to distinguish some of the $Sr_4Mn_3O_{10}$ maxima (marked with green circles) concealed by the $Sr(OH)_2$ peaks. $SrCO_3$ contamination is also detected (marked with an asterisk).

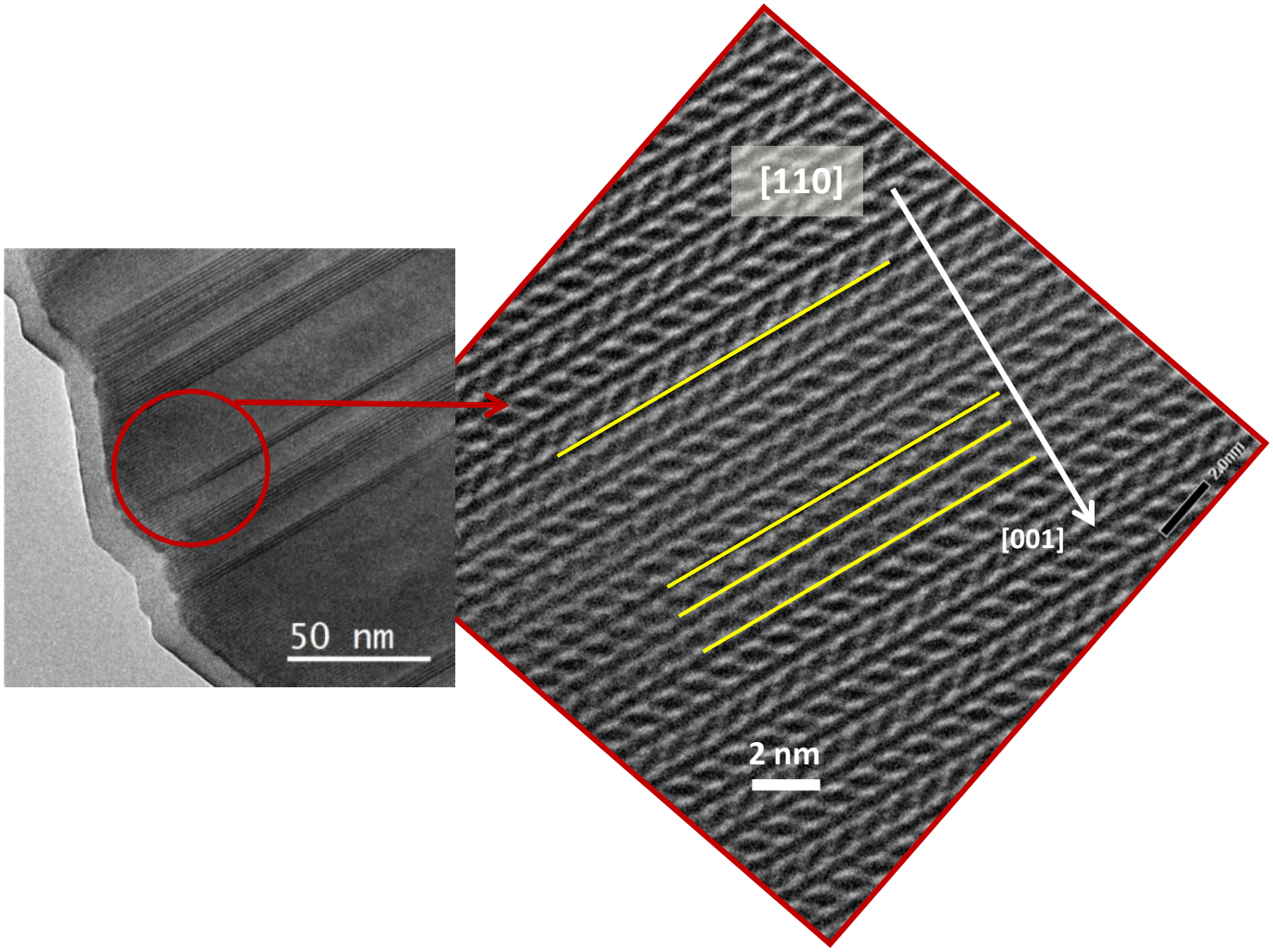

Figure S2. Low magnification TEM micrograph of a $Sr_4Mn_3O_{10}$ platelet showing twinning along (001) planes. A detailed atomic resolution image of a twin plane is shown in the enlargement.

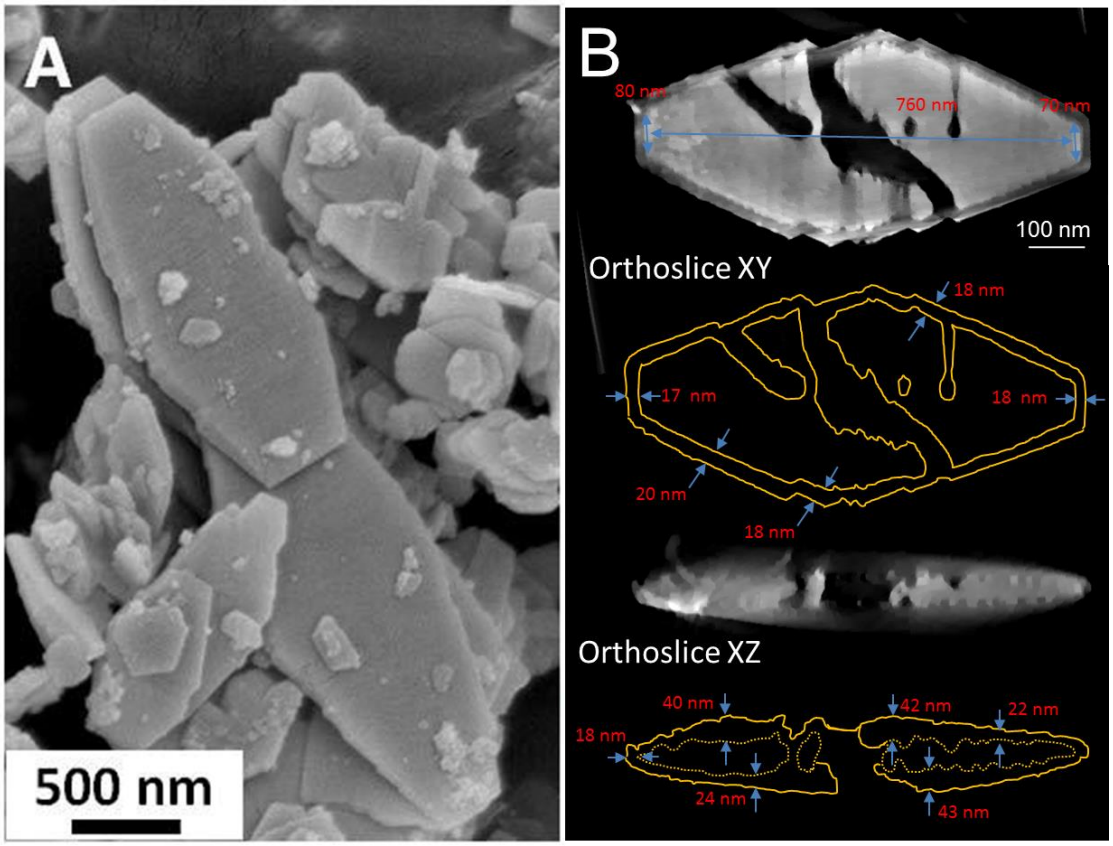

Figure S3. Topology and nanometrology of $Sr_4Mn_3O_{10}$ platelets. (A) SEM micrograph. (B) STEM-HAADF tomography. XY and XZ orthoslices from the 3D reconstruction of a $Sr_4Mn_3O_{10}$ particle and a model of its texture with distances and measurements of the thickness of the amorphous shell. 3D representations (**Figure 1M** and **Movie S1**) and SEM (**A**) show that the platelets are not flat but slightly oblong and get thinner at the edges, with thicknesses of 100 nm at the center and 20 nm at the edge. The width of the amorphous shell is ~20 nm.

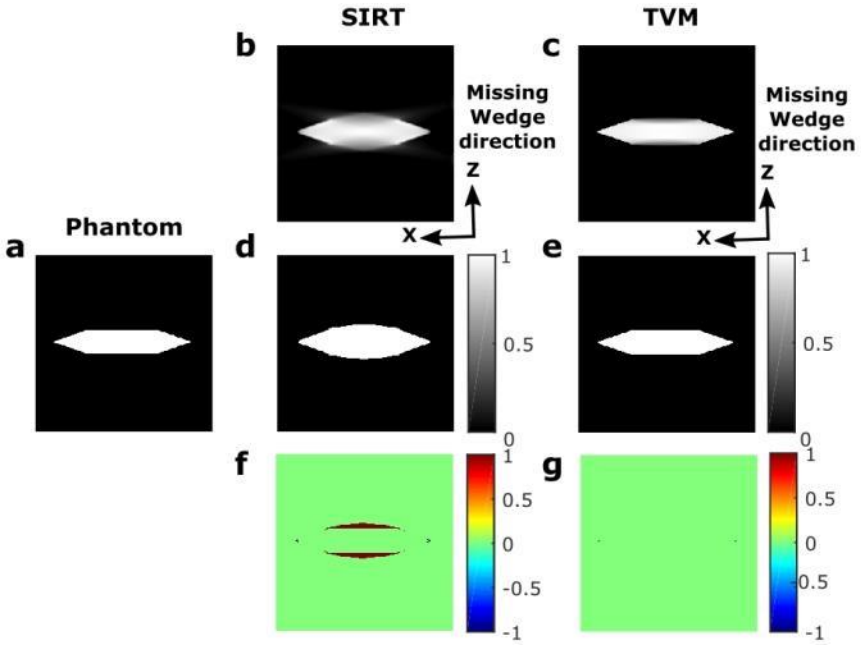

Figure S4. Transmission electron tomography: simulation of the volume reconstruction process. To test the fidelity of the tomographic reconstruction, a simple model was built (a) and re-projected from -76° to +76 ° every 2°. The model was reconstructed by two methods: (b) the well-known simultaneous iterative reconstruction technique (SIRT) using 100 iterations and (c) the Total Variation Minimization (TVM) algorithm using TVAL3 solver. Segmentation of the reconstructed model by SIRT (d) and TVM (e) was carried out automatically using the Otsu thresholding. To map the residual error, the difference between the original object and the segmented reconstruction was calculated (f-g). The limitation of the maximum tilt angle during the electron tomography acquisition results in an artificial elongation along the z axis after the volume reconstruction, called the missing wedge artifact. However, the TVM algorithm is able to reduce the artifact, thus providing a morphology closer to the original object. This is TVM reconstruction that is used in the whole manuscript.

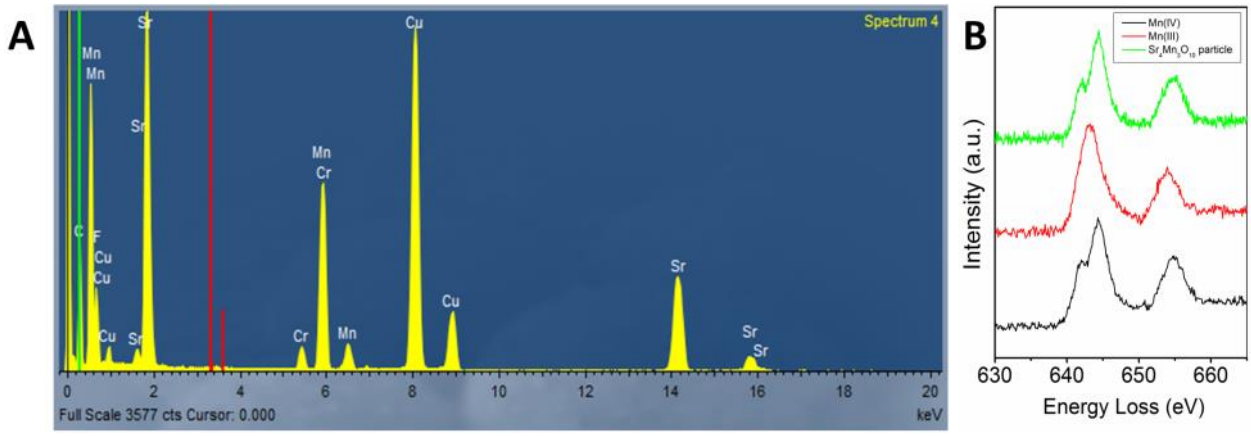

Figure S5. Analytical TEM analysis of unwashed $Sr_4Mn_3O_{10}$ platelets obtained after 1 h of heat treatment. (A) EDX and (B) EELS analyses of unwashed particles within the quenched reaction medium. In A, the C and Cu signals come from the grid, the Cr signal comes from the sample holder. The red bars in A indicate the position of the K-α lines of potassium, which is absent from the spectrum and then can be ruled out as potential impurity that would have come from the $KMnO_4$ reagent. The black and red EELS spectra in B are spectra of reference Mn^{4+} and Mn^{3+} species. The $Sr_4Mn_3O_{10}$ particles (green) are solely made of Mn^{4+}. Altogether, EDX and EELS show that the unwashed particles are pure $Sr_4Mn_3O_{10}$.

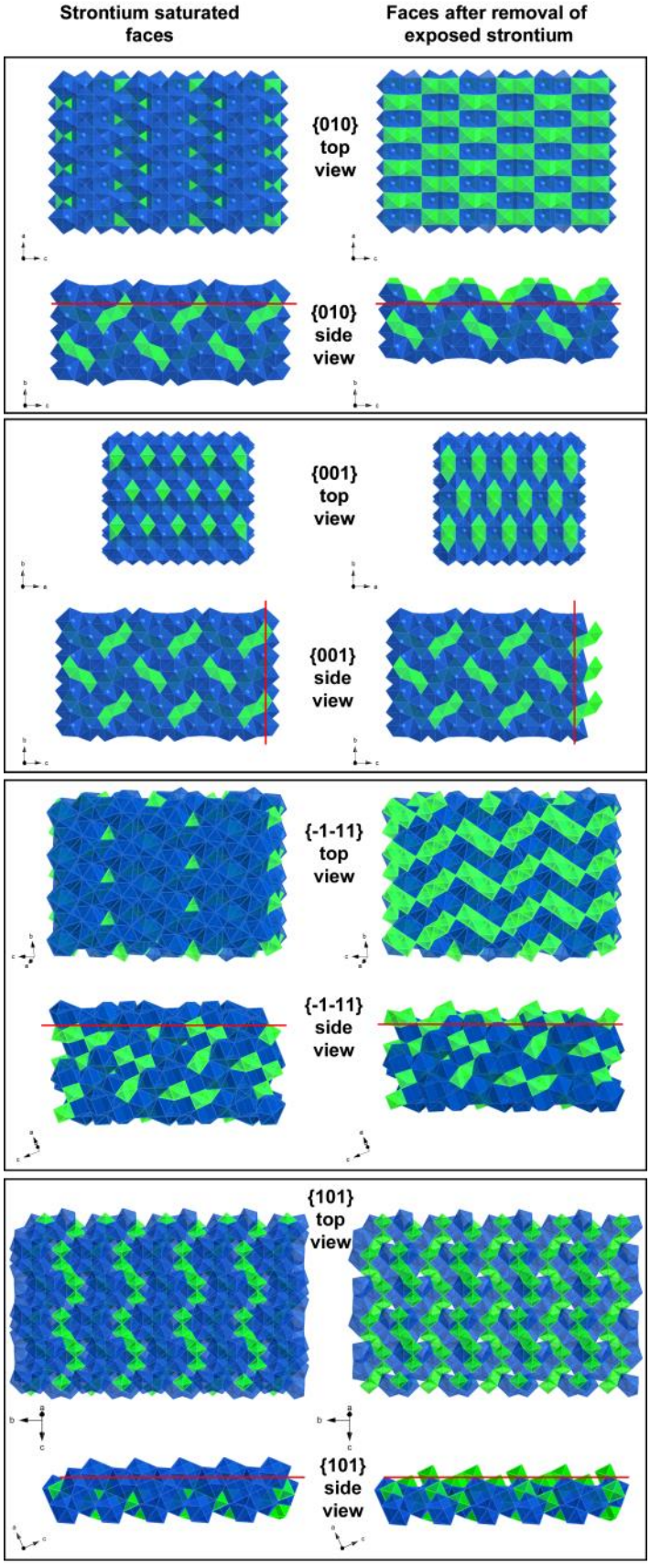

Figure S6. Exposed faces of primary particles: {010}, {001}, {-1-11}, {101} facets. MnO_6 and SrO_{10} polyhedra are pictured in green and blue, respectively. Top and side views. Left column shows most Sr-enriched slabs of each plane. Those correspond to the most probable composition of exposed facets in molten strontium hydroxide. Right column shows facets after removal of the Sr^{2+} cations exposed in the configuration of the left column.

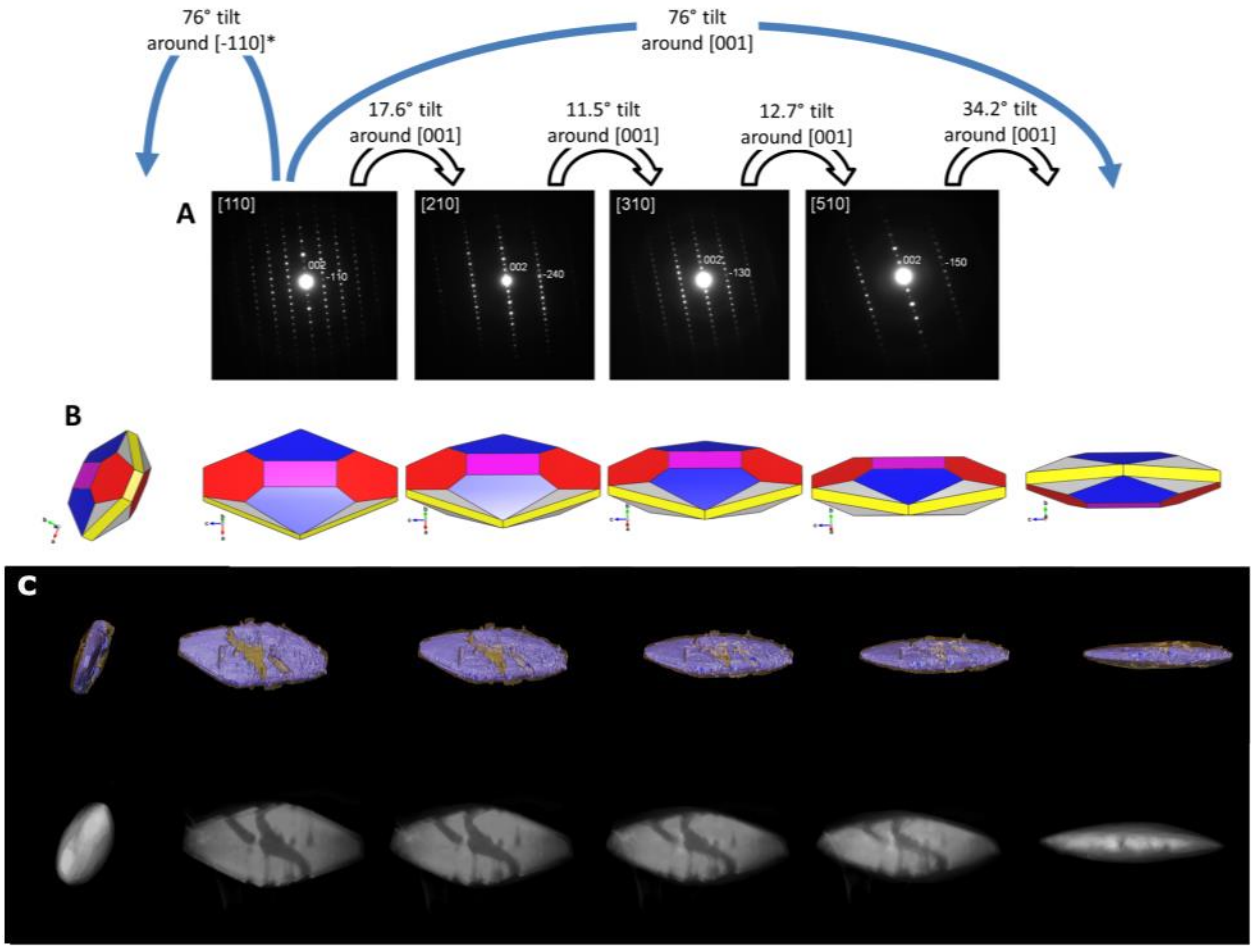

Figure S7. Tilt series acquired on a $Sr_4Mn_3O_{10}$ platelet from a sample washed after 72h of heat treatment. (A) SAED patterns; (B) corresponding projections from the morphological model and projections at the maximum experimental tilt angle of 76° around the [-110]* and [001] axes; (C) corresponding experimental projections from the STEM-HAADF tomography reconstruction.

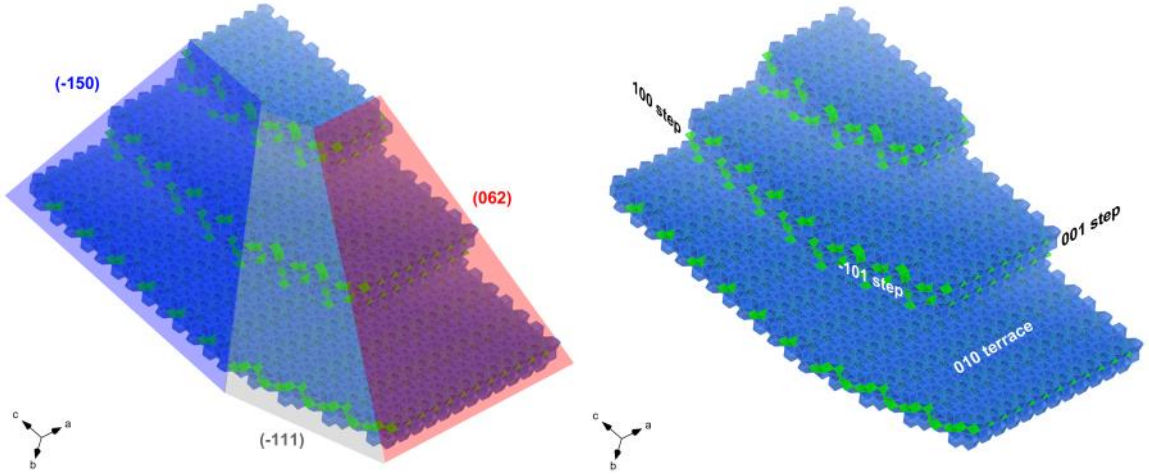

Figure S8. The basal face ({150}, {111}, {062}) of $Sr_4Mn_3O_{10}$ platelets: interpretation as (001), (100), (101)-stepwise (010) face with the most Sr-enriched configuration. MnO_6 and SrO_{10} polyhedra are pictured in green and blue, respectively.

MUSIC^2 model

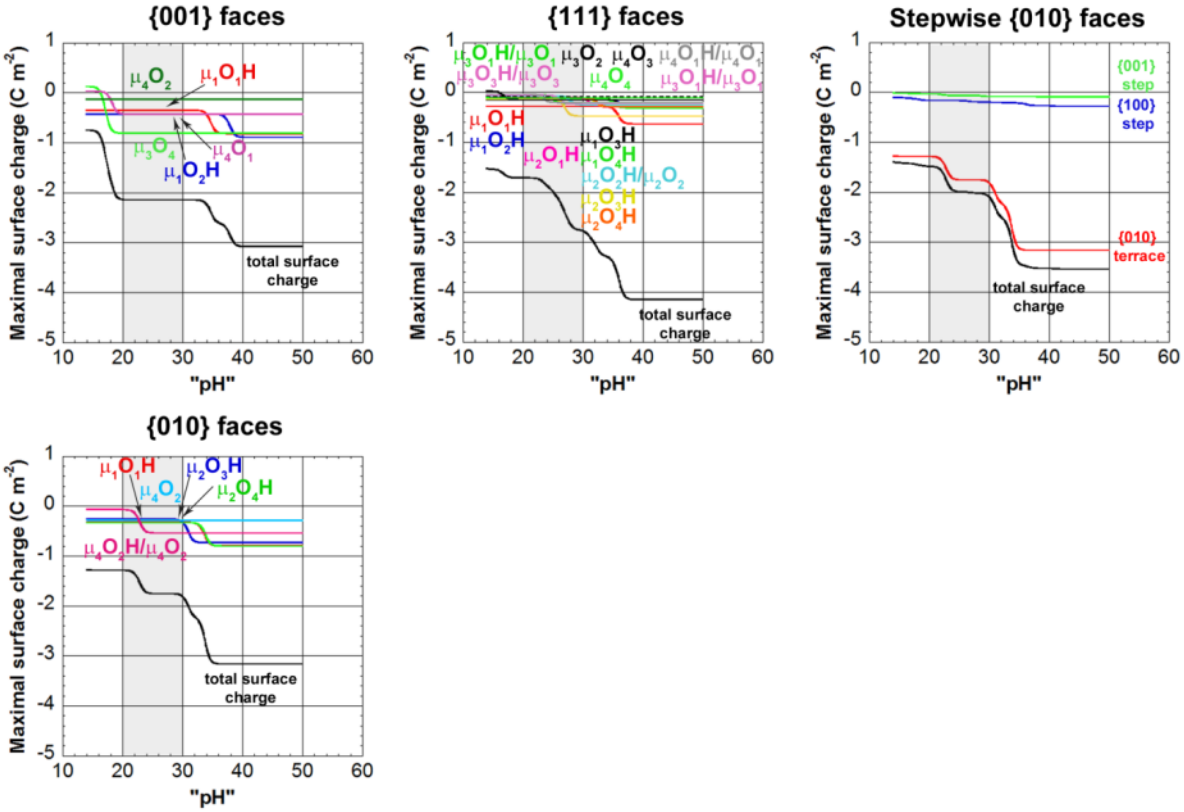

Figure S9. Maximal surface charges evaluated according to the MUSIC^2 model. See the "methods" section for the significance of "pH" in the molten hydroxide medium. The grey area is the most probable area corresponding to experimental conditions of particles growth. In the synthesis conditions (**SI**), {001} and {111} faces possess similar surface charge while stepwise {010} basal faces exhibit the lowest charge. Note that the occurrence of steps does not change significantly the charge of the basal face, so that eventual {101} steps (**Figure S9**) are omitted.

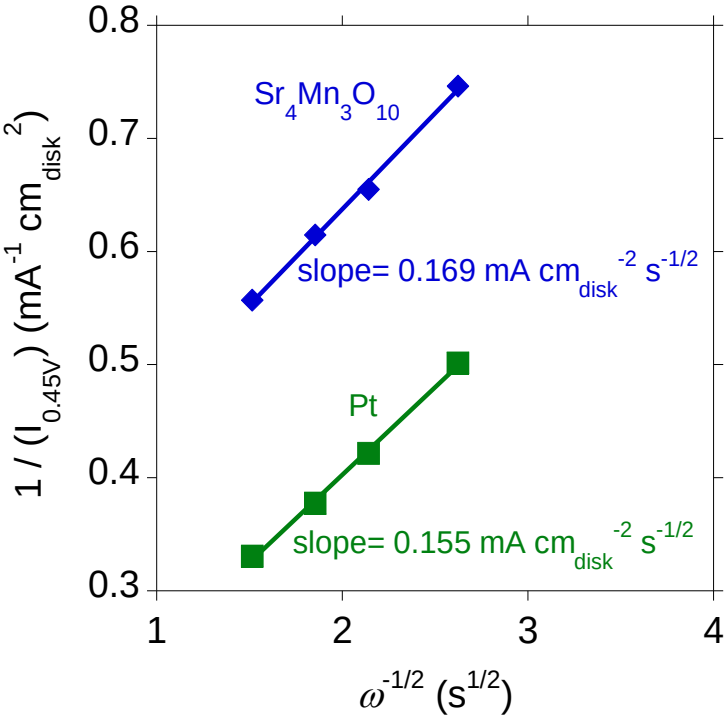

Figure S10. Koutecky-Levich plots for the oxygen reduction reaction on commercial Pt/C catalyst and on $Sr_4Mn_3O_{10}$. The slope is inversely proportional to the number of electrons involved in the reaction. The multiplication factor is independent of the catalyst, so that parallel lines indicate the same number of involved electrons (J. Suntivich, H. A. Gasteiger, N. Yabuuchi, Y. Shao-Horn, *J. Electrochem. Soc.* **2010**, *157*, B1263). Pt is known to undergo ORR by a 4 electrons reduction down to water and used as a normalizing sample. The resulting number of electrons exchanged for $Sr_4Mn_3O_{10}$ is 3.7

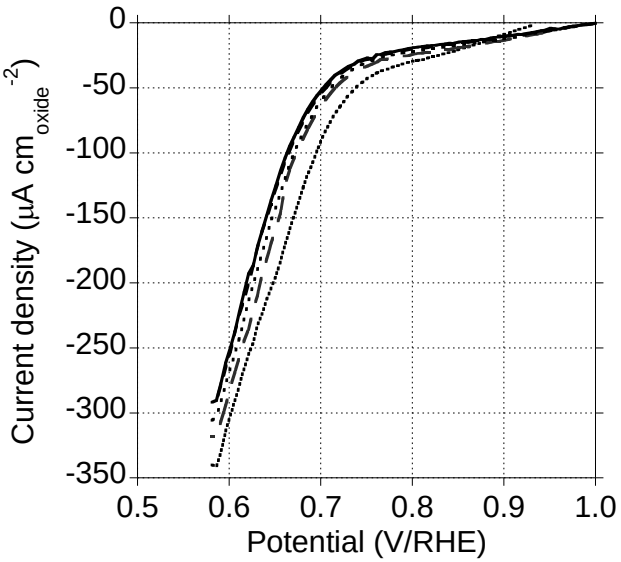

Figure S11. First 5th voltametric cycles (corrected from capacitive current) of $Sr_4Mn_3O_{10}$. After 3 cycles, the current density stabilizes at ~-280 μA cm^{-2}_{oxide}

TABLES

Table S1. Energy loss (eV) of the Mn-$L_{2,3}$ edges for $Ca_2Mn_3O_8$, $LaMnO_3$, $Ca_2Mn_3O_5$ and $Sr_4Mn_3O_{10}$.

Sample	E (eV) Mn-L_3	E (eV) Mn-L_2
Crystalline area $Sr_4Mn_3O_{10}$	644.4	654.9
Amorphous area $Sr_4Mn_3O_{10}$	641.9	653.6
$Ca_2Mn^{4+}{}_3O_8$	644.4	654.9
$LaMn^{3+}O_3$	643.2	654.0
$Ca_2Mn^{2+}{}_3O_5$	641.2	652.3

Mn-$L_{2,3}$ EELS spectra corresponding to standards as well as crystalline and amorphous areas of $Sr_4Mn_3O_{10}$ are shown in **Figure 1L.** The corresponding Mn-$L_{2,3}$ energy loss values are summarised in **Table S1.** In the crystalline areas, the high energy resolution achieved allows observing the splitting of the Mn-L_3 line in agreement with calculated octahedral environment Mn^{4+} spectrum [G. Radtke, C. Maunders, S. Lazar, F.M.F. de Groot, J. Etheridge, G.A. Botton, "The role of Mn in the electronic structure of $Ba_3Ti_2MnO_9$" *Journal of Solid State Chemistry*, 178 (2005) 3436–3440]. The energy of both L_3 (644.4 eV) and L_2 (654.9 eV) white lines are in agreement with those exhibited by Mn^{4+} in $Ca_2Mn_3O_8$ confirming that Mn is only present as Mn^{4+} in the crystalline zones of the $Sr_4Mn_3O_{10}$ particles. However, when the analysis is performed on the amorphous areas, the shift of the Mn-$L_{2,3}$ edge towards lower energies indicates a higher concentration of manganese in lower oxidation state in agreement with the observed Sr depletion in order to balance electroneutrality.